Supplementary Information

Importance of Broken Geometric Symmetry of Single-Atom Pt Sites for Efficient Electrocatalysis

Junsic Cho[1,†], Taejung Lim[2,†], Haesol Kim[1,†], Ling Meng[3], Jinjong Kim[2], Jong Hoon Lee[4], Gwan Yeong Jung[5], Francesc Viñes[3], Francesc Illas[3], Kai S. Exner[6,*], Sang Hoon Joo[2,*] & Chang Hyuck Choi[1,*]

[1]Department of Chemistry, Pohang University of Science and Technology (POSTECH), Pohang 37673, Republic of Korea.

[2]Department of Chemistry, Ulsan National Institute of Science and Technology (UNIST), Ulsan 44919, Republic of Korea.

[3]Departament de Ciència de Materials i Química Física & Institut de Química Teòrica i Computacional (IQTCUB), Universitat de Barcelona, c/ Martí i Franquès 1-11, 08028 Barcelona, Spain.

[4]UNIST Central Research Facilities (UCRF), Ulsan National Institute of Science and Technology (UNIST), Ulsan 44919, Republic of Korea.

[5]School of Energy and Chemical Engineering, Ulsan National Institute of Science and Technology (UNIST), Ulsan 44919, Republic of Korea.

[6]Faculty of Chemistry, Theoretical Inorganic Chemistry, University of Duisburg-Essen, 45141 Essen, Germany; Cluster of Excellence RESOLV, 44801 Bochum, Germany; Center for Nanointegration Duisburg-Essen (CENIDE), 47057 Duisburg, Germany.

†These authors contributed equally to this work.

*Corresponding authors: (K.S.E) kai.exner@uni-due.de; (S.H.J) shjoo@unist.ac.kr; (C.H.C) chchoi@postech.ac.kr

Experimental details

Preparation of the Pt_1/CNT catalysts

Before synthesizing the catalysts, multiwalled carbon nanotubes (CNTs; MR99, Carbon Nano-material Technology Co., Ltd.) with an average diameter of 10 nm and an average length of 10 μm were heated and subsequently acid washed to remove metallic impurities[1,2]. In detail, CNTs (38.0 g) were calcined at 500 ℃ for 1 h in a box furnace at a heating rate of 7.9 ℃ min^{-1}. The heat-treated CNT powder was then acid washed at 80 ℃ for 12 h in 810 g of 6 M HNO_3 (diluted from 60% HNO_3, Samchun Chemicals) under vigorous stirring. After filtration and washing with excess deionized (DI) water, the powder was treated with 720 g of 6 M HCl (diluted from 36% HCl, Samchun Chemicals) as described above. The acid-treated CNTs were collected after drying overnight in an oven at 60 ℃.

Pt_1/CNT catalysts with various Pt contents (Pt_1(X)/CNT, where X = nominal wt.% of Pt) were synthesized by solid-state mixing of CNT and Pt-macrocycle precursor following by annealing[3]. The acid-treated CNT (500 mg) and Pt^{II} meso-tetraphenylporphine (PtTPP, 95%, Frontier Scientific) were ground in an agate mortar over 20 min until the color and texture became constant. The PtTPP contents in the precursor mixtures were 71.0, 21.6, and 2.1 mg for Pt_1(3)/CNT, Pt_1(1)/CNT, and Pt_1(0.15)/CNT, respectively. Subsequently, the powder mixture was pyrolyzed at 700 ℃ for 3 h under an N_2 flow (5N, 1 L min^{-1}) at a heating rate of 2.1 ℃ min^{-1}. N-doped CNT was synthesized by a similar method, but with 54.0 mg of TPP (1−3% Chlorin, Frontier Scientific), which is equivalent to 71.0 mg of PtTPP, was used as a precursor.

Two model catalysts with abundant oxygen (O-Pt_1(3)/CNT) or chlorine (Cl-Pt_1(3)/CNT) functionalities were prepared by post-treatment of Pt_1(3)/CNT. O-Pt_1(3)/CNT (150 mg) was prepared by ozone treatment at 25 ℃ for 1 h using an ozone generator (LAB-I, Ozonetech Inc.). Cl-Pt_1(3)/CNT was prepared by sequential H_2O_2 and SO_2Cl_2 treatments[4]. Pt_1(3)/CNT (75 mg) was mixed with a 12.7 wt.% H_2O_2 solution (1.5 L; diluted from 29–32% H_2O_2, Alfa Aesar) and the mixture was stirred at 70 ℃ for 2 h. The catalyst powder was collected by filtration and washed several times with DI water. Subsequently, H_2O_2-treated Pt_1(3)/CNT (70 mg) was dispersed in 4.2 mL of acetonitrile (99.8%, Sigma-Aldrich) and 280 mg of SO_2Cl_2 (97%, Sigma-Aldrich) was added. The mixture was stirred for 2 h at 75 ℃ and subsequently, heated and refluxed for 5 h at 75 ℃. Cl-Pt_1(3)/CNT was collected *via* filtration and washed several times with DI water.

Physical characterizations

High-angle annular dark-field scanning transmission electron microscopy (HAADF-STEM) images were obtained using a Titan^3 G2 60-300 microscope (FEI Company) equipped with a double-sided spherical aberration (Cs) corrector operated at an accelerating voltage of 200 kV. X-ray diffraction (XRD) patterns were obtained using a high-power X-ray diffractometer (D/MAX2500V/PC, Rigaku) equipped with Cu Kα radiation operated at 40 kV and 200 mA. The XRD patterns were measured in the 2θ range from 10° to 90° at a scan rate of 2° min^{-1}. XRD samples were prepared by pelletizing 50 mg of the catalyst in a sample holder (13 mm in width) under 8 tons of hydraulic pressure. X-ray photoelectron spectroscopy (XPS) measurements were performed using a K-Alpha spectrometer (Thermo Fisher Scientific) equipped with a monochromatic Al Kα X-ray source (1486.6 eV). XPS Pt 4f and N 1s spectra were analyzed using the XPSPeak41 software with a mixed Gaussian (70)–Lorentzian (30) function after applying Shirley-type background correction. The spin-orbit components of the XPS Pt 4f spectra were fixed at 3.34 eV. To quantify the Pt content in the catalysts, a microwave digestion system (Mars 6, CEM) was used to completely dissolve Pt in aqua regia (36% HCl:60% HNO_3 = 3:1, v/v) at 220 ℃ for 40 min (600 W, heating rate of 6.7 ℃ min^{-1}). Subsequently, the resulting solution was analyzed by inductively coupled plasma-optical emission spectroscopy (ICP-OES; 700-ES, Varian).

Pt L_3-edge X-ray absorption spectroscopy (XAS) spectra were collected at the 6D beamline of the Pohang Accelerator Laboratory (PAL). The XAS spectra of the samples were obtained in the transmission mode after pelletizing the catalysts in a sample holder (1 cm in width). Background removal and normalization of the absorption coefficient for X-ray absorption near edge structure (XANES) spectra and fitting for the Fourier transformed k^3-weighted extended X-ray absorption fine structure (EXAFS) spectra were performed using the Athena and Artemis software with 1.1 of Rbkg in a Hanning-type window[5]. Crystallographic data for the PtTPP molecule were used for multishell fitting with the first-shell of Pt–N and the second-shell of Pt···C[6,7]. The amplitude reduction factor (S_0^2) of Pt was fixed at 0.84 after calibration using a standard Pt foil. For the XANES white line (WL) fitting, the interpolation plot of Pt references in our previous report was used to estimate the average oxidation number from the WL area[8].

Electrochemical characterizations

Electrochemical measurements were conducted in a conventional three-electrode H-type cell using a potentiostat (VMP3, Bio-Logic Science Inc.). A homemade rotating disk electrode (RDE) with mirror-polished glassy carbon (5 mm diameter), Pt wire (CE-100, EC Frontier), and saturated Ag/AgCl (RE-T1A, EC Frontier) electrodes were used as the working, counter, and reference electrodes, respectively. The counter electrode was separated from the working and reference electrodes using a glass frit. To prevent unexpected contamination from the reference electrode[9], it was doubly separated from the electrolyte using a glass tube equipped with a glass frit. Ar-saturated 0.1 M $HClO_4$ solutions with and without 1 M NaCl (or 1 M NH_4Cl), which were prepared using DI water (≥18.2 Ω, Arium Mini, Sartorius), concentrated $HClO_4$ solution (70%, Sigma-Aldrich), NaCl (99%, Sigma-Aldrich), and NH_4Cl (99.5%, Sigma-Aldrich), were used as electrolytes. All potentials are given relative to the reversible hydrogen electrode (RHE) scale after calibration of the reference electrode with a Pt wire electrode in an H_2-saturated electrolyte before each electrochemical measurement.

A thin-film electrode was fabricated by drop-casting the catalyst ink (10 μL) onto an RDE. The catalyst loading was 100 μg cm^{-2}. The catalyst ink was prepared by dispersing 5 mg of the catalyst in a mixed solution of DI water (2122 μL), isopropyl alcohol (374 μL), and 5 wt.% Nafion solution (50 μL). Before measuring the chlorine evolution reaction (CER) activity, the working electrode was electrochemically activated by 50 cycles of cyclic voltammetry (CV) in the potential range of 0.05–1.2 V_{RHE} at a scan rate of 500 mV s^{-1} in an Ar-saturated 0.1 M $HClO_4$ electrolyte. CER polarization curves were obtained in the potential range of 1.0–1.6 V_{RHE} at a scan rate of 10 mV s^{-1} in Ar-saturated 0.1 M $HClO_4$ with 1 M NaCl. During the measurements, the working electrode was rotated at 1600 rpm using a rotor (RRDE-3A, ALS). Durability tests were performed using 500 CV cycles in the potential range of 1.0–1.6 V_{RHE} at a scan rate of 100 mV s^{-1}. In this study, the onset potential of the CER was defined as the potential at 1 mA cm^{-2} during CER polarization. All electrochemical results were shown after 85% *iR* compensation correction, which was conducted by electrochemical impedance spectroscopy (EIS) at a fixed potential of 0.9 V_{RHE} in the frequency range of 100 kHz–1 Hz with a potential amplitude of 10 mV.

The electrochemical Cl_2 formation was analyzed by chronoamperometry (CA) using a rotating ring-disk electrode (RRDE; 012613, ALS). The CER selectivity was measured for 120 s at an electrode rotation speed of 1600 rpm; this step was repeated five times with an intermittent break of 1 min. The applied disk potential was adjusted to generate a current density

of ≥10 mA cm^{-2}, but the applied Pt ring potential was fixed at 0.95 V_{RHE}[10]. Prior to the RRDE study, the background currents of the disk and ring electrodes were stabilized at 0.95 V_{RHE} with an electrode rotation of 1600 rpm. The net CER current (i_{CER}) at the disk electrode and CER selectivity were calculated using the following equations.

$$i_{CER} = \left|\frac{i_r}{N}\right| \quad \text{(Eqn. S1)},$$

$$Cl_2 \text{ selectivity (\%)} = 100 \cdot \frac{2 \cdot i_{CER}}{i_d + i_{CER}} = 100 \cdot \frac{2 \cdot \left|\frac{i_r}{N}\right|}{i_d + \left|\frac{i_r}{N}\right|} \quad \text{(Eqn. S2)},$$

where i_r, N, and i_d denote the background-corrected ring current, collection efficiency (0.35–0.37, calibrated using $K_3[Fe(CN)_6]$), and background-corrected disk current, respectively.

Online EFC/ICP-MS measurements

Online Pt dissolution was analyzed by inductively coupled plasma-mass spectrometry (ICP-MS; iCAP RQ, Thermo-Fisher Science) coupled with a homemade electrochemical flow cell (EFC). The EFC was composed of a U-shaped channel (1 mm diameter) and two openings (3 mm diameter). On one opening side, a mirror-polished 3 mm glassy carbon electrode (002012, ALS) made electrochemical contact with the electrolyte (Supplementary Fig. 8). On the other opening side, a 3 mm Teflon tube, which was sealed with a polytetrafluoroethylene (PTFE) membrane (WP-020-80, Sumitomo Electric Ind., Ltd.) at one end, was approached to the working electrode to extract any evolved gas products by vacuum. The counter electrode was a graphite rod separated from the electrolyte by a Nafion 115 membrane (DuPont). The reference electrode was a saturated Ag/AgCl electrode that was directly connected to the outlet of the EFC. The electrolyte was Ar-saturated 0.1 M $HClO_4$ with 1 M NH_4Cl, which continuously flowed to the EFC at a flow rate of 400 μL min^{-1} (Note: we avoided using 1 M NaCl due to significant damage on the sampler and skimmer corns of the ICP-MS instrument; Supplementary Fig. 9). Prior to introducing the electrolyte to the ICP-MS instrument, it was mixed with 0.5 M HNO_3 containing 5 ppb ^{187}Re as an internal standard at a mixing ratio of 1:1 using a Y-connector. Online Pt dissolution was estimated using the ratio of ^{195}Pt to ^{187}Re signals during the electrochemical treatments. The catalyst loading on the working electrode was 100 μg cm^{-2}. After stabilizing the online ICP-MS signals for 30 min at an open-circuit potential (OCP), the working electrode was electrochemically activated by 50 CV cycles at a scan rate of 500 mV s^{-1} in the potential range of 0.05–1.2 V_{RHE}. Subsequently, Pt dissolution was monitored over 500 CV cycles at a scan rate of 100 mV s^{-1} in the potential range of 1.0–1.6

V_{RHE}.

DFT calculations

1. Computational details

Electronic structure calculations for periodically replicated appropriate models were performed using the Vienna *ab initio* simulation package (VASP 5.4.1) based on the framework of density functional theory (DFT)[11]. The exchange–correlation potential was treated as in the generalized gradient approximation (GGA) with form proposed by Perdew–Burke–Ernzerhof (PBE)[12]. The valence electron density was expanded on a plane wave basis set with an optimal kinetic energy cutoff of 415 eV, and the projected augmented wave (PAW) method[13], as implemented in VASP by Kresse and Joubert[14], was used to take into account the effect of core electrons on the valence electron density. To carry out the necessary numerical integrations in the reciprocal space, the Brillouin zone was sampled using a 4×4×1 k-point Γ-centered Monkhorst-Pack grid. A convergence criterion of 10^{-5} eV was used for the total energy, while the relaxation of atomic positions was stopped when forces acting on all relaxed atoms were smaller than 0.01 eV $Å^{-1}$. The calculation of vibrational frequencies for the optimized geometries were carried out by taking the elements of the Hessian matrix as finite differences of analytical gradients with intervals of 0.03 Å. A vacuum width of 25 Å was added to the *x*- and *y*-direction (along the plane direction defined by the employed models), whereas a vacuum width of 20 Å was added in the *z*-direction in all cases to avert artificial interactions between the periodically repeated models. An effective description of the dispersion interactions was included using the Grimme's DFT-D3 method[15]. The adsorption energy was calculated as follows:

$$E_{ads} = E_{i/sub} - (E_{sub} + E_i) \quad \text{(Eqn. S3)},$$

where E_{sub} is the energy of relaxed Pt–N_4 or Pt–N_3(V), E_i is the energy of the reference molecule, and $E_{i/sub}$ is the energy of the intermediate adsorbed on the active Pt sites of Pt–N_4 or Pt–N_3(V). Based on this definition, it follows the more negative the E_{ads} value, the more stable the adsorption structure.

The CER/OER performance was evaluated by calculating the free-energy changes (ΔG) for each elementary reaction step according to the following equation:

$$\Delta G = \Delta E + \Delta E_{ZPE} - T\Delta S \quad \text{(Eqn. S4)},$$

where ΔE corresponds to E_{ads} (*cf.* Eqn. S3), ΔE_{ZPE} is the change in zero-point energy for the

step of interest, T is the temperature in Kelvin, and ΔS is the change in entropy. ΔE_{ZPE} was obtained directly from the calculated vibrational frequencies in the harmonic approximation whereas the $T\Delta S$ term requires evaluating the vibrational partition functions which are also related to the vibrational frequencies[16].

2. Surface Pourbaix diagrams

In this study, the free energies of the intermediate structures (*Cl, *OCl, *O, *OH, and *OOH) were considered for Pt–N_4 and Pt–N_3(V). To include the applied electrode potential, U, in the analysis of free-energy changes, the computational hydrogen electrode approach (CHE) was used[17]. This was achieved by considering the stoichiometric coefficients of the transferred electrons (e^-) and protons (H^+), denoted as $\nu(e^-)$ and $\nu(H^+)$, respectively, when compiling reaction equations for each adsorption process[18]. We derive the following formula:

$$\Delta G\,(\mathrm{pH}, U) = \Delta E_{tot} + \Delta E_{ZPE} - T\Delta S - \nu(H^+)\,0.059\ \mathrm{pH} - \nu(e^-) \cdot eU \qquad \text{(Eqn. S5).}$$

The value of 0.059 eV was derived from the term $k_B T \cdot \ln 10$ evaluated at room temperature, where k_B is Boltzmann's constant and U is the applied electrode potential on the standard hydrogen electrode (SHE) scale[19].

The most thermodynamically favorable structure was determined by the minimization of the ΔG values for each adsorbate among the set of considered surface structures. The resulting surface phase (Pourbaix) diagram is shown as a function of overpotential η, defined by $\eta = U - 1.36$ V. For the analysis, the pH was fixed at zero, because we aimed to comprehend trends for the anodic CER in an acidic medium[20]. Hence, we are not discussing pH effects for which the application of grand canonical schemes is called for[21].

3. Mechanistic studies: Assessment of electrocatalytic activity

Free-energy diagrams for the CER over Pt–N_4 and Pt–N_3(V) were constructed to evaluate the CER activity of these active sites. Based on the knowledge gained in previous studies[3,8,22], the CER was assumed to proceed *via* the Volmer–Heyrovsky mechanism[23,24]. Two different Volmer–Heyrovsky pathways with dissimilar intermediates (*i.e.*, *Cl or *OCl) were considered in our theoretical study[25].

(I) Pathway mediated by the *Cl intermediate:

$$\Delta G_1: \qquad * + Cl^- (aq) \rightleftharpoons *Cl + e^- \qquad \text{(Eqn. S6),}$$

ΔG_2: $^*Cl + Cl^- (aq) \rightleftharpoons Cl_2 (g) + e^-$ (Eqn. S7).

(II) Pathway mediated by the *OCl intermediate:

ΔG_3: $^*O + Cl^- (aq) \rightleftharpoons ^*OCl + e^-$ (Eqn. S8),

ΔG_4: $^*OCl + Cl^- (aq) \rightleftharpoons ^*O + Cl_2 (g) + e^-$ (Eqn. S9).

The free energy of chloride in solution, $G (Cl^-_{aq})$, is related to that of the Cl_2 gas molecule as follows:

$Cl^- (aq) \rightleftharpoons 1/2Cl_2 (g) + e^-$, $\Delta G = 0$ eV @ $U = 1.36$ V_{SHE} (Eqn. S10).

Consequently, the ΔG_j values for each elementary step are given by:

$\Delta G_1 = -\Delta G_2 = G (^*Cl) - 1/2 \cdot G (Cl_2) - G (^*)$ (Eqn. S11),

$\Delta G_3 = -\Delta G_4 = G (^*OCl) - 1/2 \cdot G (Cl_2) - G (^*O)$ (Eqn. S12),

where $G (^*Cl)$, $G (^*O)$, and $G (^*OCl)$ are the total energies of the adsorbed intermediates and $G (^*)$ is the total energy of Pt–N_4 and Pt–N_3(V) without adsorbed intermediates. Note that the relations $\Delta G_1 = -\Delta G_2$ and $\Delta G_3 = -\Delta G_4$ are fulfilled at the CER equilibrium potential, that is, $U = 1.36$ V_{SHE}.

The oxygen evolution reaction (OER), $2H_2O (aq) \rightarrow O_2 (g) + 4H^+ (aq) + 4e^-$, $U°_{OER} = 1.23$ V_{RHE}, was modelled by assuming the mononuclear mechanism[26]:

ΔG_5: $^* + H_2O (l) \rightleftharpoons ^*OH + H^+ + e^-$ (Eqn. S13),

ΔG_6: $^*OH \rightleftharpoons ^*O + H^+ + e^-$ (Eqn. S14),

ΔG_7: $^*O + H_2O (l) \rightleftharpoons ^*OOH + H^+ + e^-$ (Eqn. S15),

ΔG_8: $^*OOH \rightleftharpoons O_2 (g) + H^+ + e^-$ (Eqn. S16).

The free energy of a proton-electron pair, $G (H^+ + e^-)$, can be related to the H_2 gas molecule using the CHE approach as follows:

$H^+ + e^- \rightleftharpoons 1/2H_2 (g)$, $\Delta G = 0$ eV @ $U = 0$ V_{SHE} (Eqn. S17).

Therefore, the ΔG values for each elementary step are:

$\Delta G_5 = G (^*OH) + 1/2 \cdot G (H_2) - G (H_2O) - G (^*)$ (Eqn. S18),

$$\Delta G_6 = G(*O) + 1/2 \cdot G(H_2) - G(*OH) \quad \text{(Eqn. S19)},$$

$$\Delta G_7 = G(*OOH) + 1/2 \cdot G(H_2) - G(H_2O) - G(*O) \quad \text{(Eqn. S20)},$$

$$\Delta G_8 = 4 \times 1.23\ \text{eV} - (\Delta G_5 + \Delta G_6 + \Delta G_7) \quad \text{(Eqn. S21)},$$

where G (*OH), G (*O), and G (*OOH) are the total energies of the adsorbed intermediates and G (*) is the total energy of Pt–N_4 and Pt–N_3(V) without adsorbed intermediates.

To quantify the electrocatalytic activity for the CER and OER, the recently introduced descriptor G_{max} (U), which is an activity measure that goes beyond the conventional approach in terms of the thermodynamic overpotential only, was used[27,28]. This descriptor relies on a free-energy span model by extracting the largest free-energy difference between intermediate states at a given target electrode potential:

$$G_{max}(U) = \max[G_{span\ \#k}(U), k = 1, \ldots, n] \quad \text{(Eqn. S22)}.$$

For further information on how to define the free-energy spans, $G_{span\ \#k}$ (U), for a two-electron (CER) or four-electron process (OER), we refer the reader to recent publications by the authors[29,30].

4. Selectivity assessment

The descriptor G_{max} (U) was extracted for both OER and CER at well-defined electrode potentials, U >1.36 V_{SHE}. The free-energy difference, G_{sel} (U), defined as

$$G_{sel}(U) = G_{max}(U)^{OER} - G_{max}(U)^{CER} \quad \text{(Eqn. S23)},$$

is a measure of the CER selectivity[31]. This quantity was used to determine the CER selectivity in percentage using the following relation[25,31]:

$$\text{CER selectivity}\ (U) = \frac{exp\left(\frac{G_{sel}}{k_B.T}\right)}{exp\left(\frac{G_{sel}}{k_B.T}\right)+1} \quad \text{(Eqn. S24)}.$$

5. Stability assessment

Considering that PtO_2 is the preferred state of Pt under CER conditions[32], the tendency of the active Pt^{II} sites toward oxidative demetallation to PtO_2 was analyzed for Pt–N_4 and Pt–N_3(V). More precisely, the free-energy change, ΔG_{stab}, for the equation [Pt] + $2H_2O$ → [ ] + PtO_2 + $4H^+ + 4e^-$ was determined by DFT. Here, [ ] denotes the empty pocket of the Pt–N_4 and Pt–N_3(V) moieties. Based on the obtained ΔG_{stab} value, the equilibrium dissolution potential, U_{diss},

was calculated as follows:

$$U_{\mathrm{diss}} = \frac{\Delta G_{\mathrm{stab}}}{4} \qquad \text{(Eqn. S25).}$$

The U_{diss} value indicates the electrode potential at which the oxidative demetallation of central Pt species to PtO_2 becomes thermodynamically favorable. Adequate stability of the Pt–N_4 and Pt–N_3(V) sites is provided if the U_{diss} value significantly exceeds the CER equilibrium potential (*i.e.*, 1.36 V_{SHE}).

Supplementary Note 1

Physical characterization of $Pt_1(X)/CNTs$

HAADF-STEM analysis was performed to identify the atomic distribution of the Pt species on $Pt_1(X)/CNT$. The results showed a uniform distribution of atomically dispersed Pt species without appreciable amounts of Pt clusters or nanoparticles (Supplementary Fig. 1). The Pt contents of $Pt_1(3)/CNT$, $Pt_1(1)/CNT$, and $Pt_1(0.15)/CNT$ were 3, 1, and 0.15 wt.%, respectively, confirmed by ICP-OES. In the XRD spectrum, $Pt_1(3)/CNT$ (and $Pt_1(1)/CNT$ and $Pt_1(0.15)/CNT$) exhibited an almost identical XRD pattern to that of a Pt-free CNT-supporting substrate (Supplementary Fig. 2). More evidently, the k^3-weighted Pt L_3-edge EXAFS spectra revealed a strong scattering peak at approximately 2.0 Å (Supplementary Fig. 3), which corresponds to Pt–N bonding. Their fitting parameters further confirmed the first-shell Pt–N bonding and second-shell Pt–C bonding without any Pt–Pt bonding. The coordination number of the Pt–N bonding for $Pt_1(3)/CNT$ was approximately four (Supplementary Table 1). Both the XANES and XPS spectra verified that the oxidation state of the Pt species on $Pt_1(3)/CNT$ was Pt^{II} (Supplementary Figs. 4 and 5). Therefore, these physical characterization results revealed that $Pt_1(3)/CNT$ was composed of abundant porphyrin-like $Pt^{II}–N_4$ moieties covalently embedded on the CNT support.

Supplementary Figures

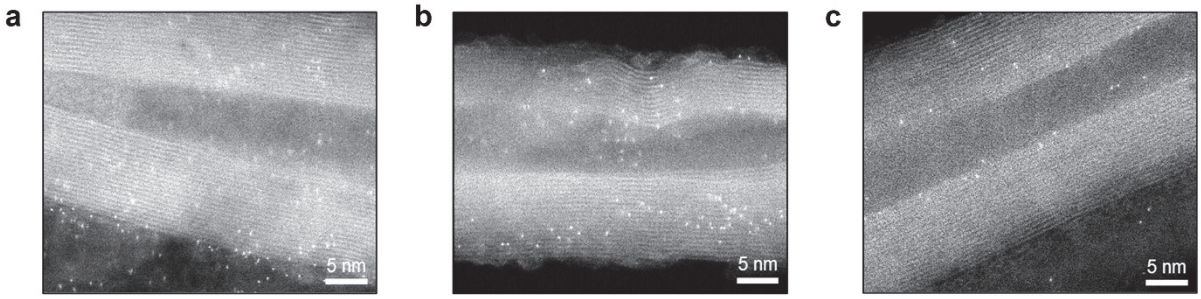

Supplementary Fig. 1: a–c, HAADF-STEM images of $Pt_1(3)$/CNT (**a**), $Pt_1(1)$/CNT (**b**), and $Pt_1(0.15)$/CNT (**c**).

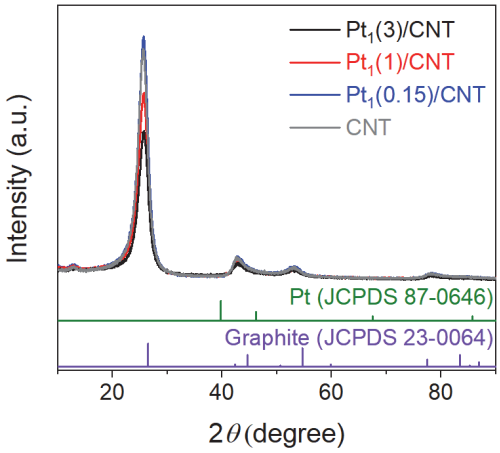

295

296 **Supplementary Fig. 2:** XRD patterns of the Pt_1(X)/CNT catalysts and CNT supporting
297 substrate. For better comparison, XRD patterns of graphite (JCPDS 23-0064) and Pt (JCPDS
298 87-0646) are also shown.

299

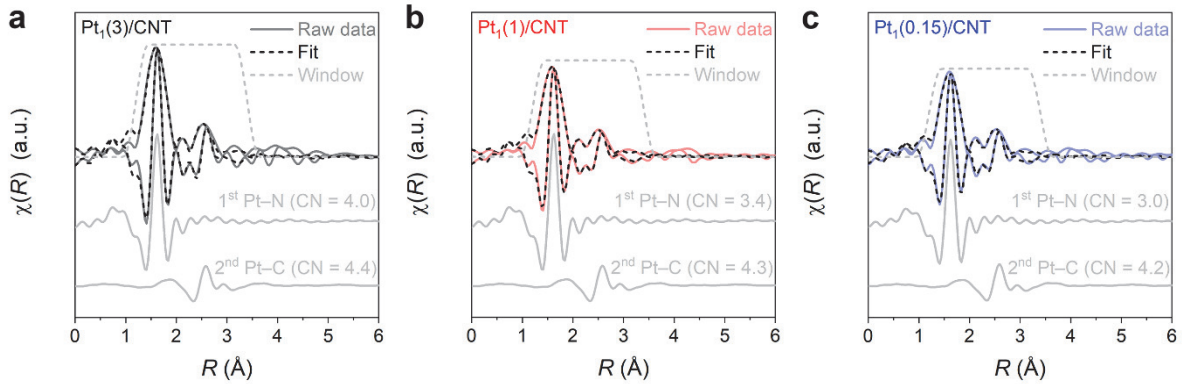

Supplementary Fig. 3: a–c, The k^3-weighted Pt L_3-edge EXAFS spectra and fitted curves of $Pt_1(3)$/CNT (**a**), $Pt_1(1)$/CNT (**b**), and $Pt_1(0.15)$/CNT (**c**). The detailed fitting parameters are provided in Supplementary Table 1.

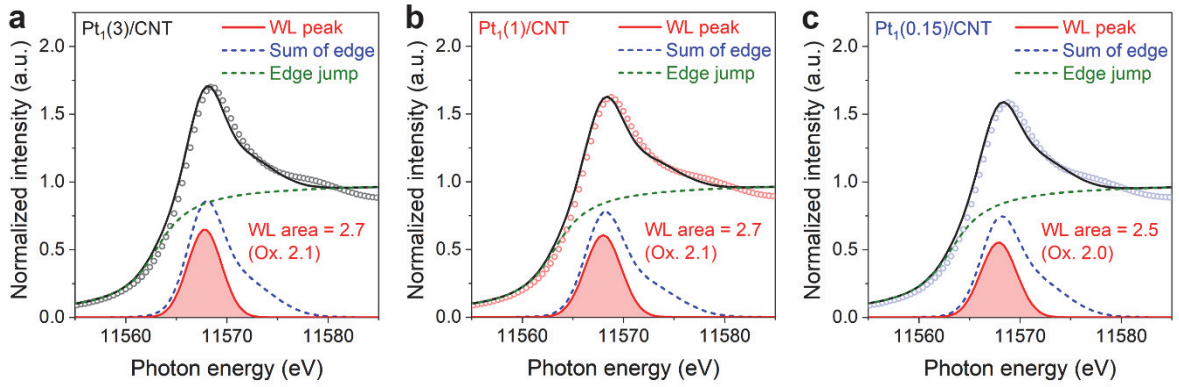

305

306 **Supplementary Fig. 4: a–c**, Pt L_3-edge XANES spectra of $Pt_1(3)$/CNT (**a**), $Pt_1(1)$/CNT (**b**),
307 and $Pt_1(0.15)$/CNT (**c**). The results show that average oxidation state of the catalysts is Pt^{II}. The
308 XANES WL fitting was conducted using the interpolation equation of Pt references in our
309 previous report[8].

310

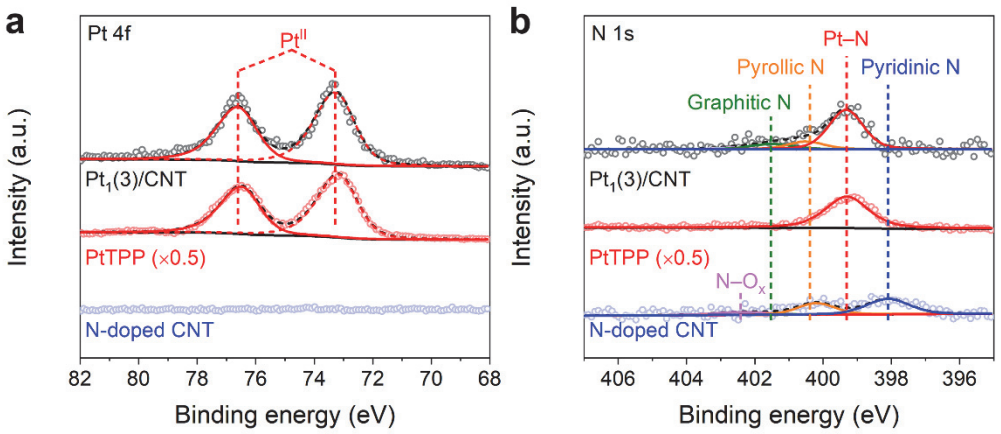

311

312 **Supplementary Fig. 5: a**, XPS Pt 4f and **b**, N 1s spectra of $Pt_1(3)$/CNT, PtTPP, and N-doped
313 CNT. The XPS Pt $4f_{7/2}$ spectrum of $Pt_1(3)$/CNT shows strong peaks at 73.2 and 76.6 eV, almost
314 identical to those of PtTPP with a Pt^{II} center.

315

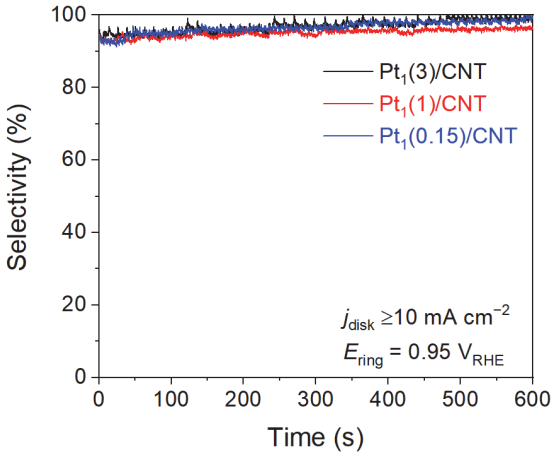

316

317 **Supplementary Fig. 6:** CER selectivity of $Pt_1(3)$/CNT, $Pt_1(1)$/CNT, and $Pt_1(0.15)$/CNT
318 measured using an RRDE in Ar-saturated 0.1 M $HClO_4$ with 1 M NaCl. The CER selectivity of
319 all the catalysts is almost 100%.

320

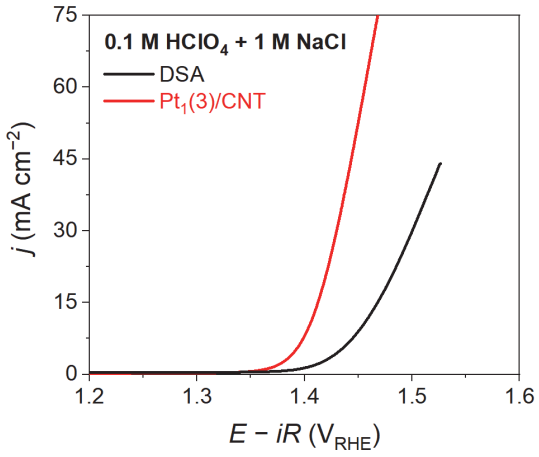

Supplementary Fig. 7: CER polarization curves of $Pt_1(3)$/CNT and Ru/Ir-based dimensionally stable anode (DSA; Ru/Ir atomic ratio = 0.5; provided by Siontech Inc.). The $Pt_1(3)$/CNT has a much higher CER activity than DSA.

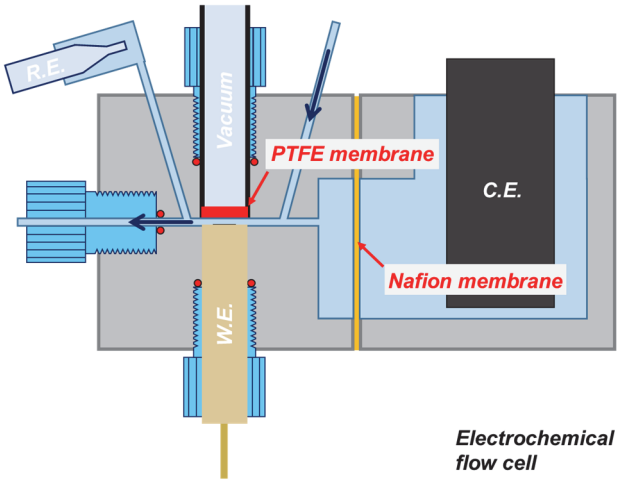

Supplementary Fig. 8: Schematic image of a homemade EFC connected to the ICP-MS. A PTFE membrane-sealed Teflon tube was installed into the EFC to remove the gaseous chlorine product by vacuum. The Nafion membrane was used to separate the counter electrode from the main body of the EFC.

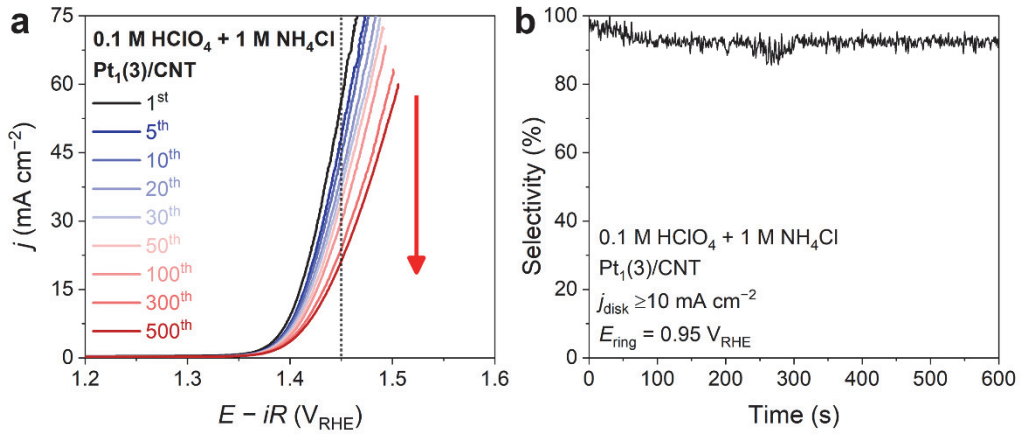

332

333 **Supplementary Fig. 9: a**, CER activity and durability measurements in Ar-saturated 0.1 M
334 $HClO_4$ with 1 M NH_4Cl. **b**, CER selectivity of $Pt_1(3)/CNT$ measured using an RRDE in Ar-
335 saturated 0.1 M $HClO_4$ with 1 M NH_4Cl. The CER activity and selectivity of $Pt_1(3)/CNT$ are
336 comparable with those measured in Ar-saturated 0.1 M $HClO_4$ with 1 M NaCl, indicating no
337 significant effects of the Cl^- precursors on the CER electrocatalysis on $Pt_1(3)/CNT$. Therefore,
338 to prevent the harmful accumulation of NaCl on the sampler and skimmer corns of the ICP-MS
339 instrument, NH_4Cl was used as a Cl^- precursor for the online EFC/ICP-MS studies.

340

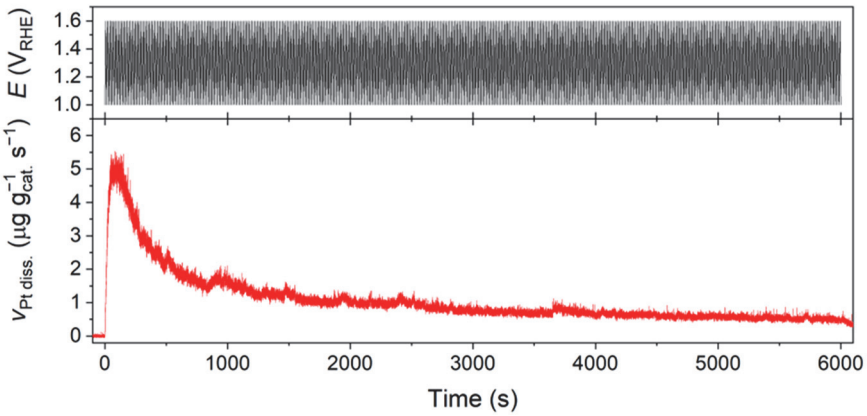

341

342 **Supplementary Fig. 10:** Real-time Pt dissolution of $Pt_1(3)$/CNT. The online EFC/ICP-MS
343 signals measured during 500 CV cycles in the potential range of 1.0–1.6 V_{RHE} in Ar-saturated
344 0.1 M $HClO_4$ with 1 M NH_4Cl.

345

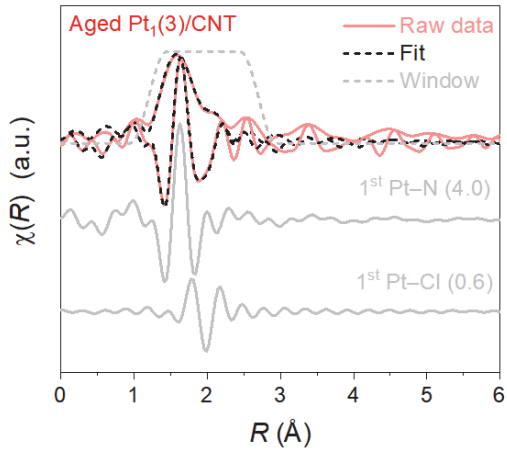

346

347 **Supplementary Fig. 11:** The k^3-weighted Pt L_3-edge EXAFS spectra and fitted curves of
348 $Pt_1(3)$/CNT after 500 CVs in the potential range of 1.0–1.6 V_{RHE} in Ar-saturated 0.1 M $HClO_4$
349 with 1 M NaCl. The detailed fitting parameters are provided in Supplementary Table 1.

350

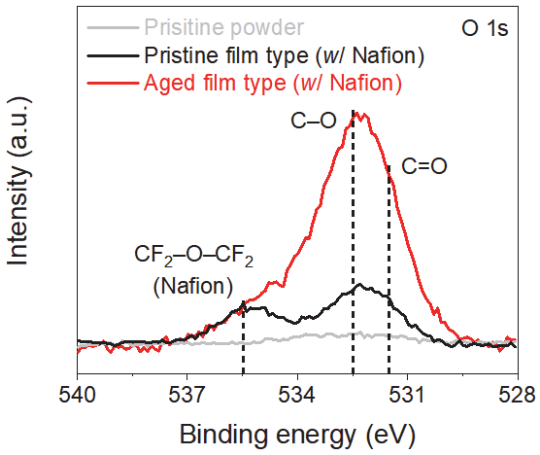

351

352 **Supplementary Fig. 12:** The XPS O 1s spectra of pristine $Pt_1(3)$/CNT powder sample, pristine
353 $Pt_1(3)$/CNT film with Nafion binder, and aged $Pt_1(3)$/CNT film with Nafion binder after 500
354 CVs in the potential range of 1.0–1.6 V_{RHE} in Ar-saturated 0.1 M $HClO_4$ with 1 M NaCl.
355 Fabrication of powder $Pt_1(3)$/CNT with the Nafion ionomer is a prerequisite for preparing the
356 working electrode. Consequently, the XPS O 1s spectrum of the aged $Pt_1(3)$/CNT film results
357 from convoluted signals of the newly generated oxygen functionalities and Nafion ionomer[33,34].
358 Thus, the XPS O 1s spectrum of the pristine $Pt_1(3)$/CNT film was subtracted from that of the
359 aged $Pt_1(3)$/CNT film to deconvolute the XPS signals of the newly generated oxygen
360 functionalities without the Nafion contribution (shown in Fig. 2a in the main article).

361

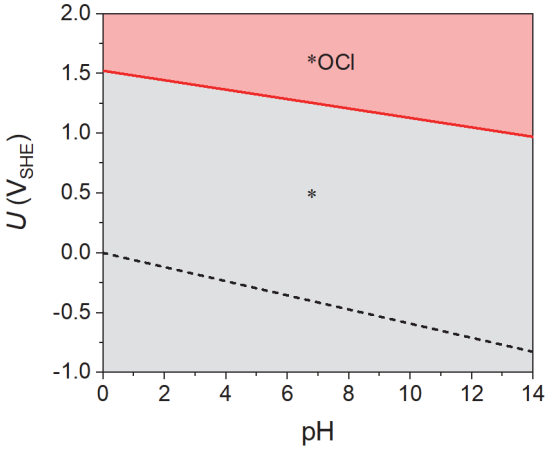

362

363 **Supplementary Fig. 13:** Surface Pourbaix diagram of the square planar Pt–N_4 model.

364

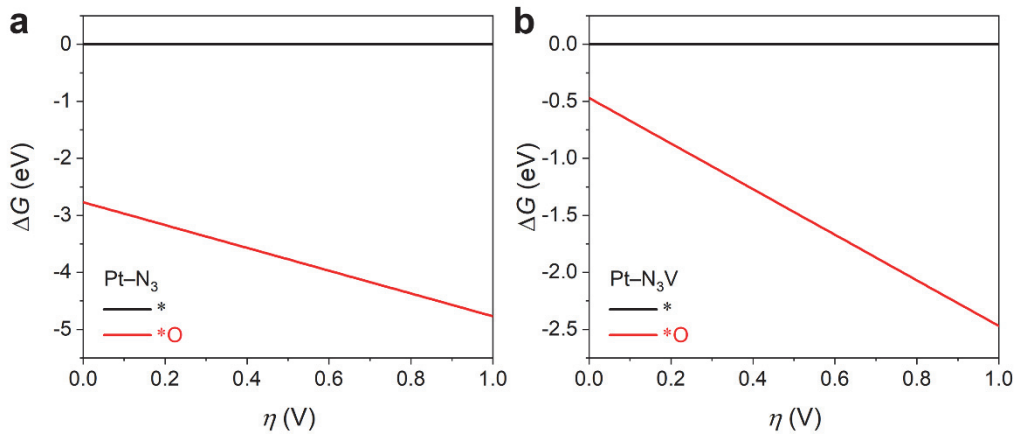

365

366 **Supplementary Fig. 14:** Pourbaix-like diagrams for the **a**, trigonal planar Pt–N_3 and **b**, T-
367 shaped Pt–N_3V models.

368

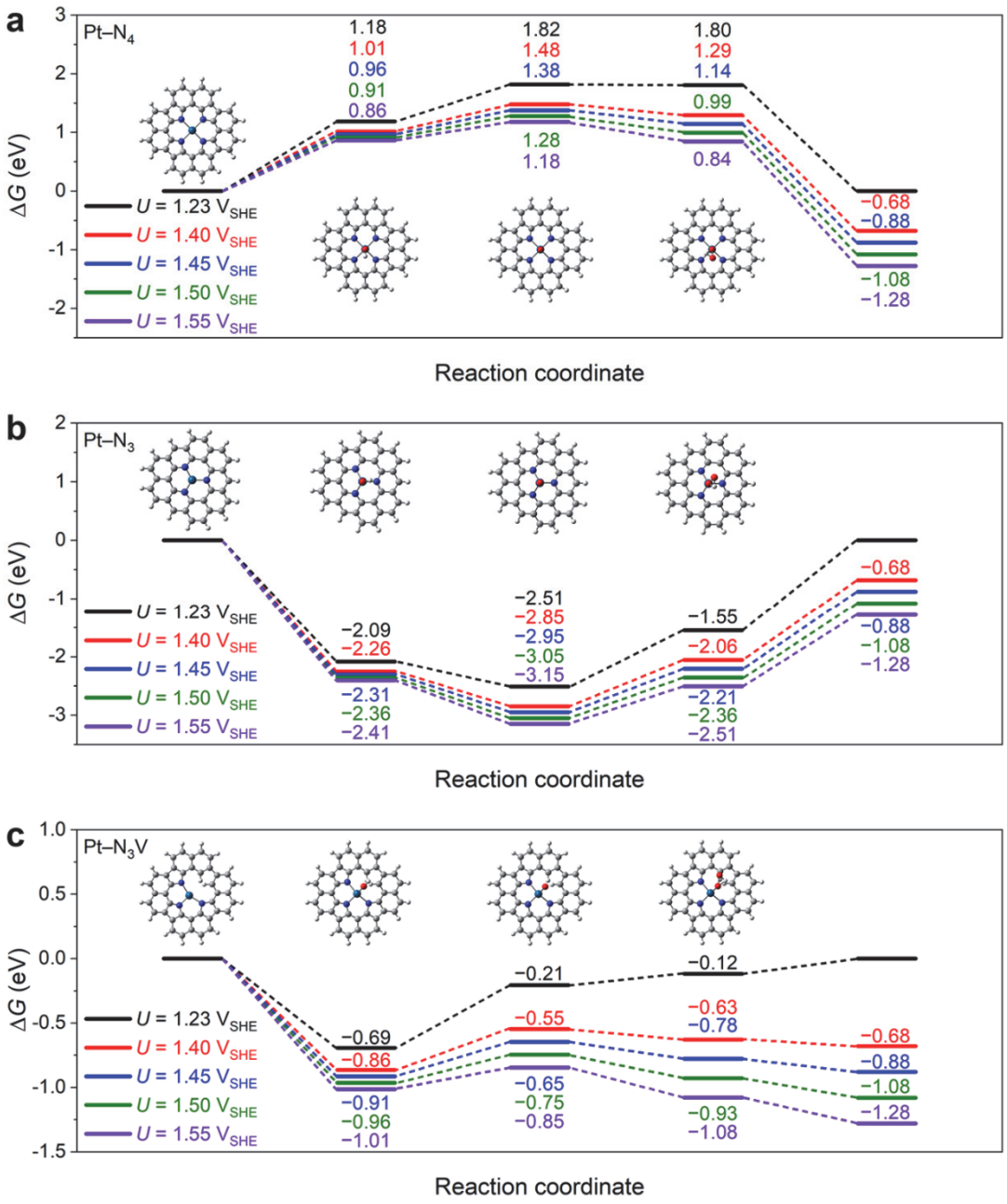

Supplementary Fig. 15: a–c, Free-energy diagrams of the OER, assuming the mononuclear mechanism *via* the *OH, *O, and *OOH adsorbates, for Pt–N_4 (**a**), Pt–N_3 (**b**), and Pt–N_3V (**c**).

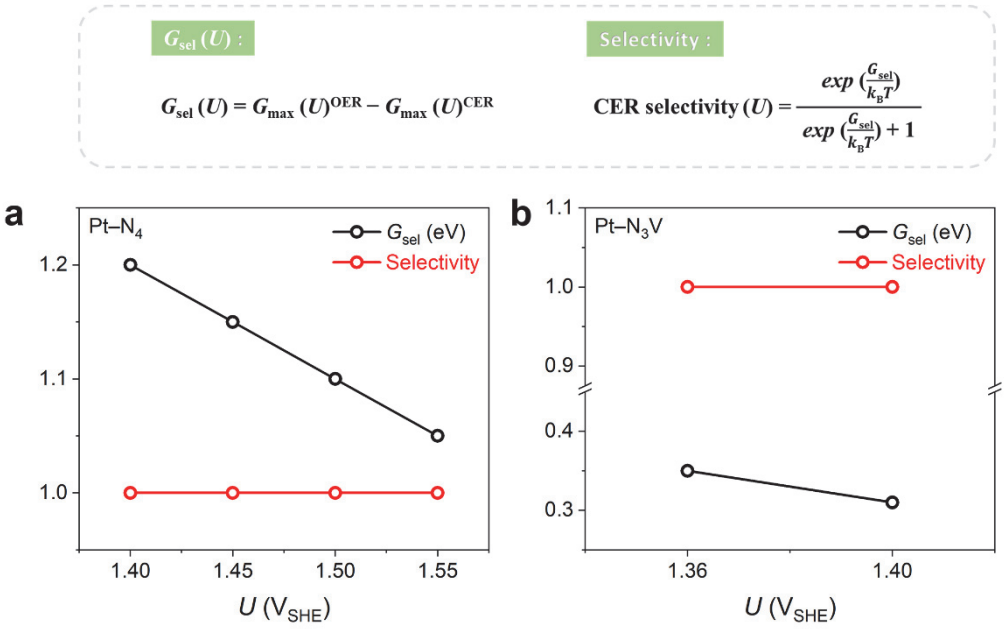

373

374 **Supplementary Fig. 16:** Selectivity analysis for the competing CER and OER processes over
375 the **a**, Pt–N_4 and **b**, Pt–N_3V sites.

376

Supplementary Table 1: Summary of EXAFS fitting parameters of pristine Pt_1(X)/CNT, aged Pt_1(3)/CNT, and Pt foil.

Sample	*k* range	R range	Shell	CN	*R* (Å)	σ^2 (10^{-3} Å^{-2})	ΔE_0 (eV)	*R* factor (%)
Pt_1(0.15)/CNT	2.7−11.2	1.2−3.4	Pt−N	3.0 (± 0.3)	2.01 (± 0.01)	3.56 (± 0.97)	16.43 (± 0.33)	1.2
			Pt···C	4.2 (± 1.3)	2.99 (± 0.02)	8.44 (± 4.01)		
Pt_1(1)/CNT			Pt−N	3.4 (± 0.4)	2.00 (± 0.01)	4.26 (± 1.00)	15.59 (± 0.91)	1.2
			Pt···C	4.3 (± 1.5)	2.97 (± 0.02)	9.38 (± 4.71)		
Pt_1(3)/CNT			Pt−N	4.0 (± 0.4)	2.01 (± 0.01)	3.58 (± 0.99)	15.89 (± 1.00)	1.3
			Pt···C	4.4 (± 1.6)	3.01 (± 0.00)	6.42 (± 4.11)		
Aged Pt_1(3)/CNT			Pt−N	4.0*	2.02 (± 0.02)	3.39 (± 0.98)	15.18 (± 2.42)	6.0
			Pt−Cl	0.6 (± 0.2)	2.33 (± 0.03)	1.00*		
Pt foil	2.1−13.5	1.7−3.8	Pt−Pt	12*	2.77 (± 0.02)	4.59 (± 0.27)	9.26 (± 0.50)	0.3

Pt−N indicates a single scattering path of the first-shell. Pt···C indicates a single scattering path of the second-shell (**Shell** column). The **CN** is the coordination number obtained from the amplitude reduction factor (S_0^2) of 0.84. ***R*** indicates bond distance. $\boldsymbol{\sigma^2}$ indicates the Debye-Waller factor. $\boldsymbol{\Delta E_0}$ indicates the energy shift. ***R* factor** was obtained from the best fit for the respective catalysts. (*Defined parameters to reduce correlations between variables)

Supplementary Table 2: Summary of G_{max} (U) for the CER and OER over Pt–N_4 and Pt–N_3 (V) at pH = 0.

G_{max} (U) (eV)	Pt–N_4	Pt–N_3	Pt–N_3V
CER	0.32[a] (0.28[b])	0.21 (0.17)	0.05 (0.01)
OER	1.56 (1.48)	2.25 (2.17)	0.35 (0.31)

[a] U = 1.36 V_{SHE}

[b] U = 1.40 V_{SHE}

Reference

1 Sa, Y. J. *et al.* A General Approach to Preferential Formation of Active Fe–N_x Sites in Fe–N/C Electrocatalysts for Efficient Oxygen Reduction Reaction. *J. Am. Chem. Soc.* **138**, 15046-15056 (2016).

2 Woo, J. *et al.* Promoting Oxygen Reduction Reaction Activity of Fe–N/C Electrocatalysts by Silica-Coating-Mediated Synthesis for Anion-Exchange Membrane Fuel Cells. *Chem. Mater.* **30**, 6684-6701 (2018).

3 Lim, T. *et al.* Atomically Dispersed Pt–N_4 Sites as Efficient and Selective Electrocatalysts for the Chlorine Evolution Reaction. *Nat. Commun.* **11**, 412 (2020).

4 Wang, C., Zhou, J. & Chu, L. Chlorine-Functionalized Reduced Graphene Oxide for Methylene Blue Removal. *RSC Adv.* **5**, 52466-52472 (2015).

5 Ravel, B. & Newville, M. ATHENA, ARTEMIS, HEPHAESTUS: Data Analysis for X-ray Absorption Spectroscopy using IFEFFIT. *J. Synchrotron Radiat.* **12**, 537-541 (2005).

6 Hazell, A. Structure of (5,10,15,20-tetraphenyl-21*H*,23*H*-porphinato)platinum(II), $C_{44}H_{28}N_4Pt$. *Acta Cryst.* **40**, 751-753 (1984).

7 Chang, Y. H., Choi, K. H., Ford, W. T., Cho, S. J. & Ryoo, R. XANES and EXAFS Study of a Platinum Phthalocyanine. *J. Chem. Soc. Chem. Commun.*, 785-788 (1994).

8 Lim, T. *et al.* General Efficacy of Atomically Dispersed Pt Catalysts for the Chlorine Evolution Reaction: Potential-Dependent Switching of the Kinetics and Mechanism. *ACS Catal.* **11**, 12232-12246 (2021).

9 Ji, S. G., Kim, H., Choi, H., Lee, S. & Choi, C. H. Overestimation of Photoelectrochemical Hydrogen Evolution Reactivity Induced by Noble Metal Impurities Dissolved from Counter/Reference Electrodes. *ACS Catal.* **10**, 3381-3389 (2020).

10 Vos, J. G. & Koper, M. T. M. Measurement of Competition between Oxygen Evolution and Chlorine Evolution using Rotating Ring-disk Electrode Voltammetry. *J. Electroanal. Chem.* **819**, 260-268 (2018).

11 Li, N. *et al.* Double Transition Metal Carbides MXenes (D-MXenes) as Promising Electrocatalysts for Hydrogen Reduction Reaction: *Ab Initio* Calculations. *ACS Omega* **6**, 23676-23682 (2021).

12 Perdew, J. P. *et al.* Atoms, Molecules, Solids, and Surfaces: Applications of the Generalized Gradient Approximation for Exchange and Correlation. *Phys. Rev. B* **46**, 6671-6687 (1992).

13 Kresse, G. & Furthmüller, J. Efficient Iterative Schemes for *Ab Initio* Total-Energy Calculations using a Plane-Wave Basis Set. *Phys. Rev. B* **54**, 11169-11186 (1996).

14 Kresse, G. & Joubert, D. From Ultrasoft Pseudopotentials to the Projector Augmented-Wave Method. *Phys. Rev. B* **59**, 1758-1775 (1999).

15 Grimme, S. Semiempirical GGA-Type Density Functional Constructed with a Long-Range Dispersion Correction. *J. Comput. Chem.* **27**, 1787-1799 (2006).

16 López, M., Exner, K. S., Viñes, F. & Illas, F. Computational Pourbaix Diagrams for MXenes: A Key Ingredient toward Proper Theoretical Electrocatalytic Studies. *Adv. Theory Simul.*, 2200217 (2022).

17 Nørskov, J. K. *et al.* Origin of the Overpotential for Oxygen Reduction at a Fuel-Cell Cathode. *J. Phys. Chem. B* **108**, 17886-17892 (2004).

18 Exner, K. S., Anton, J., Jacob, T. & Over, H. Chlorine Evolution Reaction on RuO_2(110): *Ab Initio* Atomistic Thermodynamics Study - Pourbaix Diagrams. *Electrochim. Acta* **120**, 460-466 (2014).

19 Kibsgaard, J. *et al.* Designing an Improved Transition Metal Phosphide Catalyst for Hydrogen Evolution using Experimental and Theoretical Trends. *Energy Environ. Sci.* **8**, 3022-3029 (2015).

20 Exner, K. S., Anton, J., Jacob, T. & Over, H. Controlling Selectivity in the Chlorine Evolution Reaction over RuO_2-Based Catalysts. *Angew. Chem. Int. Ed.* **53**, 11032-11035 (2014).

21 Groß, A. Reversible vs Standard Hydrogen Electrode Scale in Interfacial Electrochemistry from a Theoretician's Atomistic Point of View. *J. Phys. Chem. C* **126**, 11439-11446 (2022).

22 Exner, K. S., Anton, J., Jacob, T. & Over, H. Full Kinetics from First Principles of the Chlorine Evolution Reaction over a RuO_2(110) Model Electrode. *Angew. Chem. Int. Ed.* **55**, 7501-7504 (2016).

23 Janssen, L. J. J., Starmans, L. M. C., Visser, J. G. & Barendrecht, E. Mechanism of the Chlorine Evolution on a Ruthenium Oxide/Titanium Oxide Electrode and on a Ruthenium Electrode. *Electrochim. Acta* **22**, 1093-1100 (1977).

24 Trasatti, S. *Electrodes of Conductive Metallic Oxides, Part B (Studies in Physical & Theoretical Chemistry)*. (Elsevier Science Ltd, Amsterdam-Oxford-New York, 1981).

25 Exner, K. S. Design Criteria for the Competing Chlorine and Oxygen Evolution Reactions: Avoid the OCl Adsorbate to Enhance Chlorine Selectivity. *Phys. Chem. Chem. Phys.* **22**, 22451-22458 (2020).

26 Man, I. C. *et al.* Universality in Oxygen Evolution Electrocatalysis on Oxide Surfaces. *ChemCatChem* **3**, 1159-1165 (2011).

27 Exner, K. S. A Universal Descriptor for the Screening of Electrode Materials for Multiple-Electron Processes: Beyond the Thermodynamic Overpotential. *ACS Catal.* **10**, 12607-12617 (2020).

28 Exner, K. S. Why Approximating Electrocatalytic Activity by a Single Free-Energy Change is Insufficient. *Electrochim. Acta* **375**, 137975 (2021).

29 Razzaq, S. & Exner, K. S. Method to Determine the Bifunctional Index for the Oxygen Electrocatalysis from Theory. *ChemElectroChem* **9**, e202101603 (2022).

30 Exner, K. S. Beyond the Thermodynamic Volcano Picture in the Nitrogen Reduction Reaction over Transition-Metal Oxides: Implications for Materials Screening. *Chin. J. Catal.* **43**, 2871-2880 (2022).

31 Exner, K. S. Controlling Stability and Selectivity in the Competing Chlorine and Oxygen Evolution Reaction over Transition Metal Oxide Electrodes. *ChemElectroChem* **6**, 3401-3409 (2019).

32 Goeke, R. S., Datye, A. K., Atanassov, P. & St-Pierre, J. Model Electrode Structures for Studies of Electrocatalyst Degradation. *ECS Trans.* **33**, 361 (2010).

33 Friedman, A. K., Shi, W., Losovyj, Y., Siedle, A., R. & Baker, L. A. Mapping Microscale Chemical Heterogeneity in Nafion Membranes with X-ray Photoelectron Spectroscopy. *J. Electrochem. Soc.* **165**, H733 (2018).

34 Moulder, J. F. & Chastain, J. *Handbook of X-ray Photoelectron Spectroscopy: A Reference Book of Standard Spectra for Identification and Interpretation of XPS Data*. (Physical Electronics Division, Perkin-Elmer Corporation, 1992).